Catalysis Communications 185 (2023) 106807

Contents lists available at ScienceDirect

Catalysis Communications

journal homepage: www.elsevier.com/locate/catcom

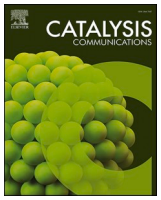

Investigating the impact of chemical structures on the photocatalytic degradation rates over ZnO nanorods: An oxidative pathways perspective

Elie A. Daher [a,b], Cédric Boissière [b], Christel Laberty Robert [b,c], Wael Hamd [d,*]

[a] Petrochemical Engineering Department, Faculty of Engineering III, CRSI, Lebanese University, Rafic Hariri Campus, 1533, Hadat, Lebanon
[b] Laboratoire Chimie de la Matière Condensée de Paris LCMCP, Sorbonne Université, UPMC Paris 06, 4 Place Jussieu, 75005 Paris, France
[c] RS2E, Réseau Français sur le Stockage Electrochimique de l'Energie, CNRS 3459, 80039 Cedex 1 Amiens, France
[d] Chemical Engineering Department, Faculty of Engineering, University of Balamand, P.O. Box 33, 1355, El-Koura, Lebanon

ARTICLE INFO

Keywords:
ZnO Nanorods
Photocatalysis
Organic pollutants
Molecular structures
Degradation rate
Pseudo-first order

ABSTRACT

Zinc oxide (ZnO) nanorods were coated on glass substrates and used as photocatalysts to evaluate the kinetic behavior of three different aromatic structures: i) single aromatic ring (phenol), ii) poly-aromatic ring (methylene blue), and iii) complex macromolecule (humic acid). The kinetics of all the tested molecules obey a pseudo-first-order model regardless of their initial concentrations. The apparent rate constants are largely controlled by the bond dissociation energy and the number of oxidation steps in each organic molecule. For instance, methylene blue presents the weakest dissociation bond energy and the highest degradation rate constant compared to humic acid and phenol.

1. Introduction

A prospering chemical industry plays a pivotal role in today's economy, contributing to 4% of global gross domestic product (GDP) and directly employing over 15 million people [1,2]. Furthermore, progressive industrial development continues to supply the main economic sectors with a diverse range of chemicals, where these substances are utilized in the production of various end products, ranging from pharmaceuticals and fertilizers to smartphones and machinery components [1]. However, when some of these chemicals reach the ecosystem, they become a major environmental concern [3]. Amongst these, phenol for example is utilized either as a raw material or an intermediate (35% of its total usage) in the synthesize a variety of products, including herbicides, paints, cosmetics, lubricants, phenolic resins, plastics, and nylons, in addition to alkylphenols and ethoxylated components [3]. However, the phenolic molecule is broadly known for its acute toxicity and recalcitrant nature, posing significant harm when released into the environment [4].

Conversely, humic acid (HA) is a macromolecule of polymeric phenolic structure, classified as a natural organic matter (NOM) and widely found in soil and surface water [5]. The substance has been mainly known for its important role in soil fertility, and in chemical industries such as the production of concrete, ceramics, plastics, and papers [6]. However, the presence of these molecules in water supplies is highly undesirable because they display a high sorbing capacity for other pollutants in aquatic mediums, and increase the level of total organic pollution [7]. For instance, their reaction with halogen-based oxidants leads to the formation of trihalomethanes (THM) with potential carcinogenic effects [8]. HA is also known for inducing cytotoxicity in many mammalian cells, growth retardation, and apoptosis in fibroblasts [9].

Methylene blue (MB) is a hetero-polyaromatic dye of wide industrial application, however, because the molecule is non-biodegradable, its accumulation in aquatic mediums could increase its toxicity to harmful levels [10]. In addition, the molecule was recently found to be toxic and carcinogenic [11].

On the other side, due to the recalcitrant nature of these molecules, conventional treatment techniques (flocculation, coagulation, activated carbon, chemical precipitation, biodegradation, and filtration) and established recovery processes (evaporation, solvent extraction, ionic exchange, membrane separation/bioreactors, and electrochemical) have proven to be quite inefficient [12]. In this context, advanced oxidation processes (AOPs) such as photochemical oxidation, catalytic wet oxidation, sonochemical oxidation, ozone (O_3) oxidation, electrochemical oxidation, Fenton oxidation, and photocatalysis are considered advantageous and cost-effective technologies for treating a wide

* Corresponding author.
E-mail address: wael.hamd@balamand.edu.lb (W. Hamd).

https://doi.org/10.1016/j.catcom.2023.106807
Received 5 July 2023; Received in revised form 11 November 2023; Accepted 15 November 2023
Available online 17 November 2023

spectrum of recalcitrant organic molecules in aquatic environments [13]. Particularly heterogeneous photocatalysis, a technique that is based on harvesting light energy, has been rapidly gaining attention [14,15]. Generally, the system generates electron-hole (e^- - h^+) pairs when a semiconducting material is exposed to a light source [15]. These electron-hole pairs are known for their capability of producing highly reactive oxygen species (ROS) such as hydroxyl radical ($OH^\bullet$) and superoxide radical ($O_2^{\bullet-}$) with strong oxidation ability towards organic matter [13]. This process leads to the total mineralization of the organic compounds into less harmful compounds such as water (H_2O) and carbon dioxide (CO_2) [13]. Therefore, secondary disposal treatments are not required.

The photocatalytic degradation of these molecules is mainly governed by several parameters, such as the pH, molecules' initial concentrations, light source/intensity, and the presence of electron/hole scavengers [16]. Although the effect of such parameters on the degradation kinetics has been extensively studied in numerous works [16–18], to the best of our knowledge, no one has reported yet on how the difference in molecular structures and bond energy impact the rate of decomposition. In this sense, as each molecule follows a specific degradation pathway, the resulting oxidation steps will determine the apparent rate constant. In this work, we present a comparative degradation study of different molecular structures over zinc oxide (ZnO) nanorods (NRs) deposited on glass substrates by a hydrothermal growth method. The purpose of immobilizing the photocatalyst is to prevent the agglomeration of NRs and to eliminate the need for a recovery step at the end of photocatalysis. In addition, the choice of ZnO nanorods is supported by the non-polar characteristic of the majority of its surface, which exhibits low selectivity towards polar molecules [19]. For this reason, the kinetic data was extracted from the photocatalytic degradation of i) single aromatic ring (phenol, molecular weight (M.W.) = 94.11 g/mol), ii) poly-aromatic rings (MB, M.W. = 319.85 g/mol), and iii) complex macromolecules (HA, M.W. > 1000 g/mol).

2. Experimental section

2.1. Chemicals

Analytical grade Zinc acetate dihydrate (Zn $(CH_3COO)_2{\cdot}2H_2O$) (97%), Zinc nitrate hexahydrate (Zn $(NO_3)_2{\cdot}6H_2O$), and Hexamethylenetetramine ($(CH_2)_6N_4$) were purchased from ACROS organics Spain. Phenol detached crystals (99+ %) were obtained from Fischer Scientific U.K. Humic Acid (technical grade) was obtained from Sigma–Aldrich Canada. Methylene Blue (laboratory reagent) was obtained from Paskem, India.

2.2. Synthesis of ZnO NRs on glass substrate

ZnO NRs were coated on microscope glass slides (4.5 cm × 2.5 cm) by a hydrothermal growth process [20]. First, the glass substrates were successively cleaned with soap water, ethanol, acetone, and deionized water (DI). Then, a ZnO layer was seeded on top of the preheated substrates at 350 °C, by spraying 10 mM zinc acetate in DI water (25 ml) at a flow rate of 1 ml/min, as seen in Scheme 1. Subsequently, the seeded substrates were soaked in a chemical bath at 90 °C, containing equimolar concentrations (10 mM) of zinc nitrate hexahydrate as a precursor and hexamethylenetetramine as a nanostructuring agent. The bath was replenished with both solutions every 5 h, and this cycle was repeated 3 times. The as-grown NRs were thoroughly washed with DI water and post-heated in the air at a temperature (T) = 350 °C for 1 h to ensure the removal of any remaining organic compounds within the metal oxide structure.

2.3. Characterization techniques

The crystalline structure of the ZnO films was analyzed with a D8 Discover X-ray diffractometer, equipped with a copper (Cu) emitter anode (K-alpha (Kα) emissions, Kα1 and Kα2 of wavelength (λ) 1.54056 and 1.5444 Å respectively) and a 1D LYNEXEYE XE-T detector (Bruker).

The surface morphology and the film's thickness were evaluated by a field emission gun scanning electron microscope (FEG-SEM) model MIRA 3 TESCAN, set to a voltage of 15 kV.

The nanostructure and the lattice fringes' spacing were examined by a transmission electron microscope (TEM) model TWIN 120 (TECNAI SPIRIT) equipped with a JEOL 100CF apparatus and coupled with selected area electron diffraction (SAED). Energy-dispersive spectroscopy (EDS) was acquired in Scanning transmission electron microscopy (STEM) mode.

X-Ray Photoelectron Spectroscopy (XPS) analyses were performed using an Omicron Argus X-ray photoelectron spectrometer, equipped with a monochromated AlKα radiation source (hν = 1486.6 eV) and a 280 W electron beam power. The emission of photoelectrons from the sample was analyzed at a photoelectron collection angle of 45^0 under ultra-high vacuum conditions (≤ 10–9 mBar). Spectra were carried out with a 100 eV pass energy for the survey scan and 20 eV pass energy for core levels regions. Binding energies were referenced to the carbon (C) 1 s peak due to carbon bound to only carbon and hydrogen at 284.8 eV and element peak intensities were corrected by Scofield factors. The peak areas were determined after subtraction of a U 2 Tougaard background. The spectra were fitted using Casa XPS software (Casa Software Ltd., U. K.) and applying a Gaussian/Lorentzian ratio g/l equal to 70/30 for deconvolution.

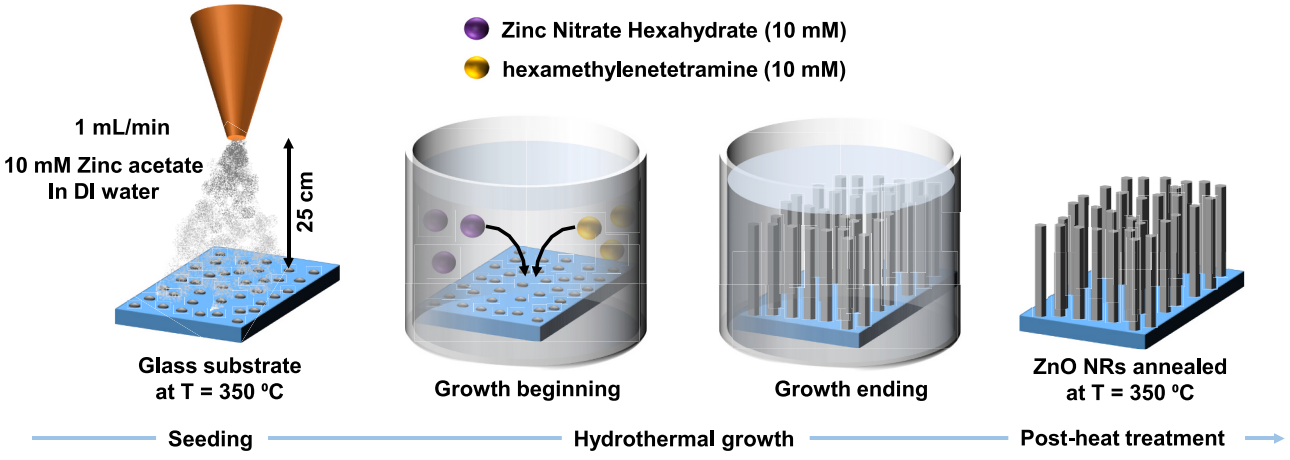

Scheme 1. Synthesis procedure of the ZnO nanorods.

The functional groups at the film's surface were analyzed by Fourier-transformed infrared (FTIR) in attenuated total reflection (ATR) mode with an incidence angle of 45^0 and a 4 cm^{-1} resolution using a Spectrum 400 model from PerkinElmer, equipped with an FR-DTGS detector (fast recovery Deuterated Triglycine Sulfate detector).

The absorbance of the deposited ZnO nanorod films and the tracking of the degradation of organic molecules were performed at room temperature by using a Specord 50 plus ultraviolet (UV)-visible spectrophotometer from Analytic-Jena, Germany.

2.4. Set-up of the photocatalytic system

The as-prepared ZnO (NRs) films were immersed inside Pyrex photocatalytic reactors of 50 ml, filled with 45 ml of MB, phenol, and HA aqueous solutions, respectively. Three different concentrations of 5, 10, and 20 ppm were used for each molecule. In all cases, the dipped area of the films corresponds to 10 cm^2. The photocatalytic reactors were initially kept in the dark for 12 h to demonstrate the insignificant adsorption of the polar molecules at the non-polar surface of the ZnO NRs. The photocatalytic tests were carried out at room temperature (RT) for 6 h using an ultraviolet A (UVA) lamp of $\lambda = 365$ nm. The light source was placed at 5 cm from the photocatalyst surface. The received illuminance by the photocatalysts was measured by a Testo 450 luxmeter of ±3% precision (from Testo, France) and found to be equal to ~500 lx. The photocatalytic degradation of the organic molecules was tracked by UV–visible spectroscopy with a sampling interval of 1 h.

3. Results and discussion

3.1. ZnO NRs microstructure

3.1.1. Morphology

A field emission gun scanning electron microscope was used to evaluate the films' microstructure. Fig. 1a reveals well-aligned nanorods with respect to each other. All the rods are characterized by hexagonal shapes, straight sides, and regular ends (Figs. 1a & b). The lengths, and

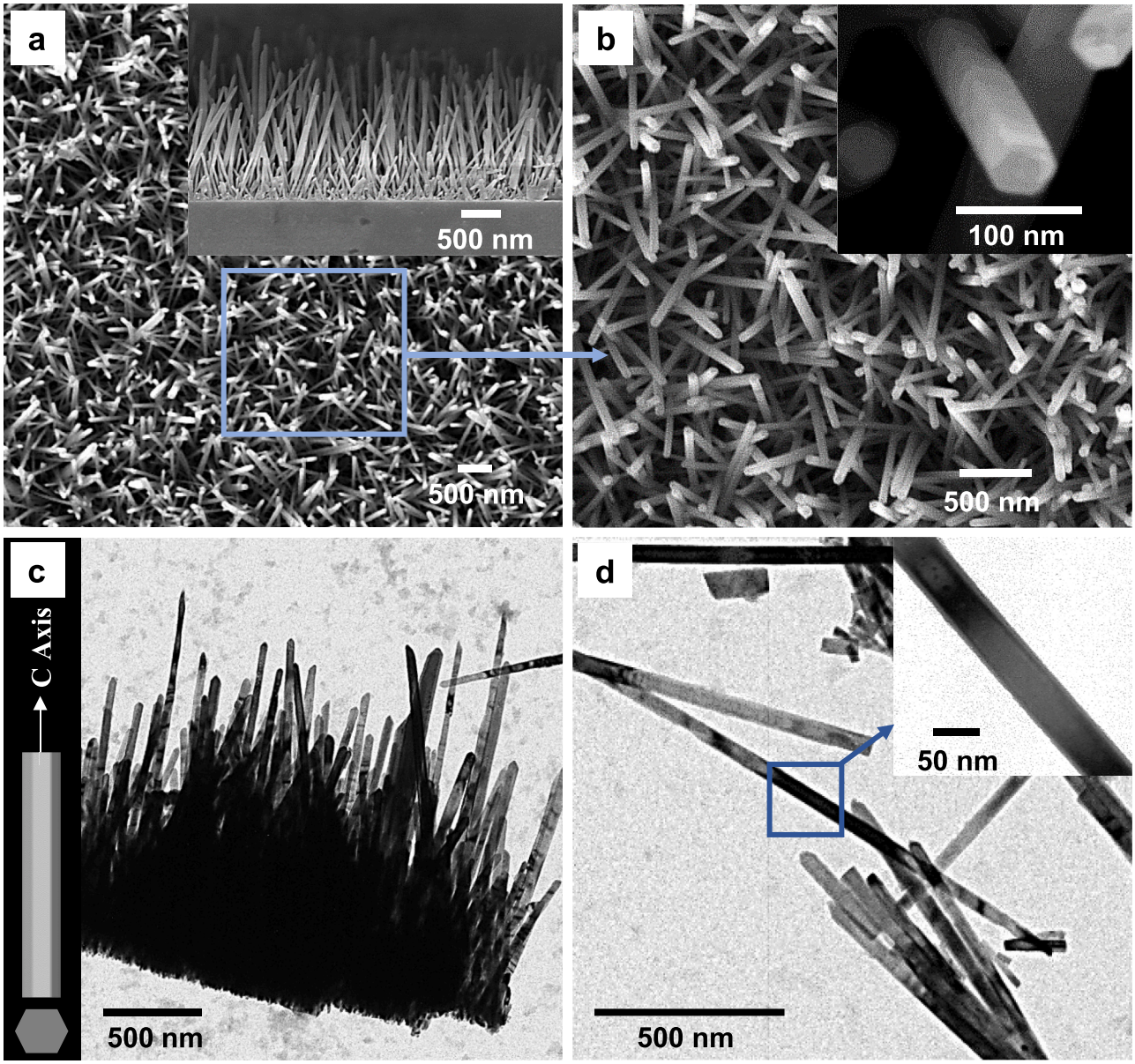

Fig. 1. **(a)** SEM top view image for ZnO NRs after post-heat treatment in the air at 350 °C for 1 h. Inset: Cross-sectional view of "a", **(b)** High magnification view of "a". Inset: Nanorods with a common hexagonal shape, **(c)** TEM images of an extracted bush-like fragment from the ZnO film of "a". Inset: Schematic illustration of a grown rod in the +c direction, **(d)** Free-standing ZnO nanorod separated with sonication. Inset: Zoomed-in view of "d".

diameters of ZnO NRs were estimated by analyzing the SEM micrographs with ImageJ software. For that purpose, the rods' boundaries were carefully highlighted by a threshold segmentation step to identify them. As a result, the nanorods are characterized by an average diameter (w) of ~ 50 nm (population standard deviation σ = 4.7 nm), a length (l) of ~ 1.55 μm (population standard deviation σ = 0.14 μm), and a remarkably high ratio of l:w ~ 31. Moreover, the average film's thickness is found ~1.38 μm.

The morphology was further investigated using transmission electron microscopy. Fig. 1c shows a typical low-magnification TEM image of an intact section that was finely extracted from the ZnO film. As can be seen, each nanorod exhibits a uniform diameter along its entire length, indicating anisotropic growth along the +c-axis direction (inset of Fig. 1c). Moreover, the individual rods appear to be well-faceted along the ±c-axis (Fig. 1d) with highly defined crystal boundaries and very few surface defects (inset of Fig. 1d).

The EDS spectrum of ZnO nanorods confirms the presence of zinc (Zn), and oxygen (O) elements of the ZnO NRs, in addition to the Cu and C components of the TEM grid (Fig. S1a). Consequently, an atomic ratio Zn:O of ~0.38:0.62 (± 0.017) is detected, deviating from the stoichiometric ratio of 1:1, and therefore indicating the potential presence of defects [21]. The elemental distribution of Zn and O within the NRs is shown in Fig. S1c & d. Furthermore, the surface states of ZnO NRs were studied using X-ray photoemission spectroscopy. The distribution of the Zn 2p in Fig. S2a shows two centered peaks at ~1021.2 eV and ~ 1044.4 eV, corresponding to the Zn $2p_{3/2}$ and Zn $2p_{1/2}$ (correlated with the Zn—O bonding) [22]. However, the fitted O 1 s by three Gaussian components, reveals 3 centered peaks; O_a (530.5 eV), O_b (531.7 eV), and O_c (532.7 eV); attributed to Zn—O bonding, O^{2-} ions in oxygen-deficient regions, and chemisorbed H_2O molecules (or dissociated O_2 or OH species on the surface of ZnO), respectively (Fig. S2b) [23]. The binding energy component at 531.7 eV (oxygen deficiency) accounts for almost 43% of the O 1 s spectrum. These defects can increase the number of trapped electrons/holes, leading to the formation of hydroxyl radical ($OH^{\bullet}$), superoxide radical ($O_2^{\bullet-}$), and other oxygenated radical species. These radicals are highly efficient in degrading organic pollutants in water [23]. Furthermore, the XPS analysis demonstrates an O content of ~38.6%, higher than that of the Zn (~ 23.1%), and in good agreement with the EDS measurements (similar Zn:O ratios are obtained).

3.1.2. Surface area

Because the Brunauer–Emmett–Teller (BET) technique requires both destructive the removal of the thin film and a large sample size (over 100 coated glass substrates), the exposed surface area (SA) of the ZnO nanorod films was estimated from Eq. 1 [24]. This estimation assumes that all the rods are characterized by a regular hexagonal shape.

$$SA = \left[\frac{1}{4}\left(3\sqrt{3}\,w^2\right) + 3wl\right]d \quad (1)$$

where w, l, and d refer to the average diameter, the average length, and the average density of the nanorods (counting per μm^2), respectively. The latter was obtained from the analysis of the SEM micrographs as previously depicted (~5.5 NRs/μm^2). Therefore, a SA of ~ 350 cm^2 was measured, corresponding to a 10 cm^2 coated substrate. After measuring this surface area, the film was carefully extracted with a fine blade and weighted with an analytical balance. As a result, a specific surface area of ~25 m^2/g was obtained, which is quite comparable to its observed counterpart on synthesized material with similar procedures [24] and threefold higher than that of commercial ZnO nanorods [25]. Moreover, the obtained SA is higher than most of the reported values for different microstructures of ZnO such as tetrapods [25], flower-like microparticles [26], nanowires [27], macroporous foam [28], and porous thin films [29]. Although hollow sphere ZnO films exhibit a relatively higher SA, their fabrication procedure is quite complex and expensive, in addition to the requirement of carbon-based templates [30]. The synthesis approaches, type of nanostructure, and surface areas of ZnO coatings in this work and other recent studies are listed in Table 1.

3.1.3. Crystalline structure

The XRD data of the as-synthesized ZnO nanorods show a characteristic pattern of hexagonal wurtzite crystal structure confirmed by the JCPDS No. 01–086-3978 with a = b = 3.248 Å and c = 5.202 Å (Fig. 2a) [23]. The strongest diffraction at 34.46^0 demonstrates a preferential orientation along the (002) crystal plane, confirming the anisotropic growth in the +c-axis direction. The formation of this nanostructure during the hydrothermal-growth mechanism is primarily directed by the hexamethylenetetramine structuration agent (non-polar). It was suggested that this molecule preferentially chelates and covers the non-polar sides of the hexagonal rods, leaving, therefore, its top polar facet exposed for growth [31]. Consequently, this process leads to the formation of ZnO nanorods with high crystallinity.

Additionally, the TEM images in Fig. 2b (lower inset) clearly reveal that the crystal boundaries are well-defined and characterized by regular lattice fringes of 0.262 nm. This value corresponds to the interplanar spacing of d_{002} and further supports the nanorods' preferential orientation in the (002) direction. The SAED pattern on the other side came to combine altogether regularly organized dots that correspond to the (002) growth direction with a weakly pronounced circular ring representing the (103) plan (Fig. 2b (upper inset)). This agrees well with the XRD measurement.

Besides the well-known impact of the crystallinity on the photoactivity of ZnO, another important factor that significantly affects it, is the material texturization [13]. Therefore, mono-crystal ZnO with a low-defected surface was reported to exhibit superior photocatalytic activity, making it a good candidate for the removal of organic contaminants [23].

3.1.4. Surface functions

The vibrational behavior of Zn—O bonds was characterized by FTIR spectroscopy and plotted in Fig. 3. The spectrum of zinc oxide nanorods shows 4 functional groups located at 540, 750, 895, and 1063 cm^{-1}.

The strong absorption peaks at ~540 and 750 cm^{-1} represent the stretching vibrations of Zn—O bonds [32] and thus confirm the formation of zinc oxide coatings. In addition, it was suggested by da Silva-Neto et al. that the observed peak in the region of 895 cm^{-1} is mainly associated with the tetrahedral coordination of Zn within the wurtzite ZnO lattice [33]. The weakest peak at ~1063 cm^{-1} mainly arises from the C—O stretching vibration band of chemisorbed organic molecules at the film's surface [34]. This confirms the need for annealing the as-synthesized films at $T > 350$ °C.

3.1.5. Optical properties

The optical properties of the films were determined at various steps of the synthesis of ZnO i) after deposition of seeded particles: ii) after

Table 1
Synthesis approaches and surface areas of ZnO coatings with different morphologies.

Reference	Synthesis Approach	ZnO micro/ nanostructure	Surface-Pore diameter
Sulciute et al. [25]	combustion method	Tetrapods	~22 m^2/g
Pugliese et al. [26]	hydrothermal process	Flower-like nanoparticles	~20 m^2/g
Gu et al. [27]	Hydrothermal method	Nanowires	~10.4 m^2/g
Kovačič et al. [28]	High Internal Phase Emulsion Technique	Macroporous foam	~5.5 m^2/g
Smith et al. [29]	Magnetron sputtering	Porous thin films	~ ~ 11.8 m^2/g
Zhang et al. [30]	Template-based method with carbon microspheres	Hollow spheres	~ 37 m^2/g
This study	**Hydrothermal method**	**Nanorods**	**~ 25 m^2/g**

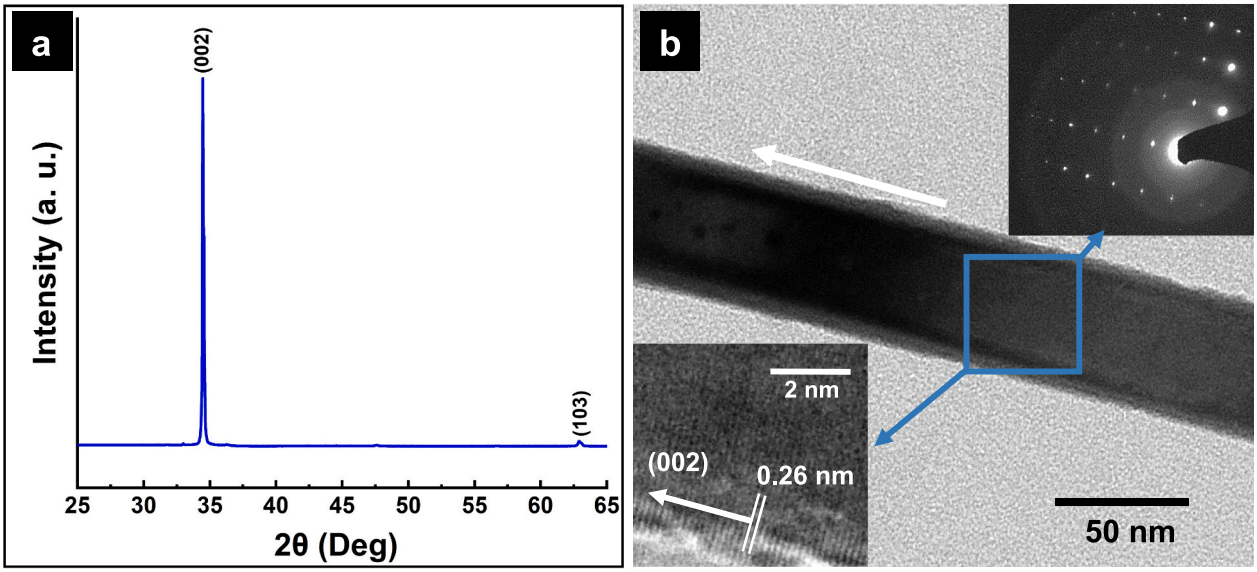

Fig. 2. (a) XRD pattern of ZnO NRs after post-heating in the air at 350 °C for 1 h, **(b)** TEM image of a free-standing ZnO nanorod. The insets show a high magnification area of "b" and its SAED respectively.

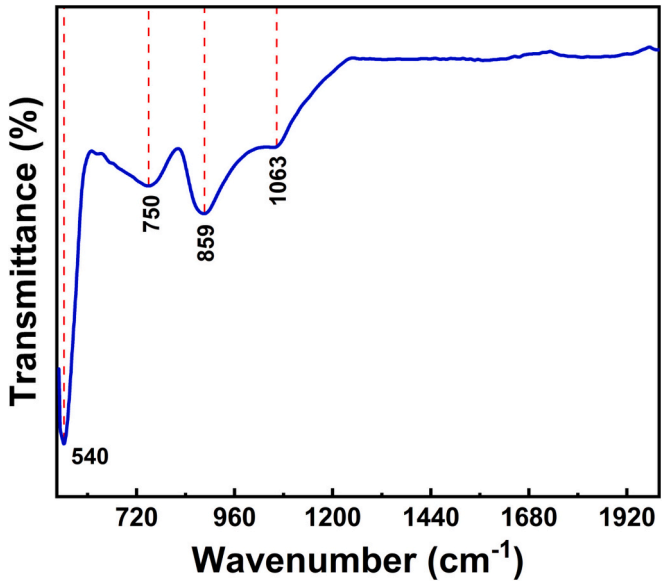

Fig. 3. ATR-FTIR spectrum of the ZnO NRs after post-heating in the air at 350 °C for 1 h.

drying the as-grown ZnO nanorods at RT, and iii) after annealing the nanorods at 350 °C. As seen in Fig. 4a, the seeded ZnO layer (black curve) shows a significant absorption in the UV region <400 nm corresponding to its intrinsic bandgap energy [35].

As the ZnO nanorods are grown and the film thickens, the absorbance intensity strongly increases by ~ 10 times at λ = 367 nm. This surge is accompanied by the appearance of a weak absorption area in the visible region from 400 to 800 nm (red curve). Such a progressive increase in the absorption profile from the visible to UV range is probably due to the film's diffusivity (Inset Fig. 4a). Moreover, the effect of heat treatment on the nanorods resulted in a slight increase in the light absorbance below 400 nm. This behavior is probably due to the complete removal of chemisorbed organic precursors and the fine enhancement in crystallinity (blue curve) [36]. The optical band gap (Eg) of ZnO was also calculated at each of the synthesis stages. For this reason, the first derivative of the absorbance with respect to photon energy (dA/dE), was plotted as a function of photon energy (E) (Fig. 4b) [37]. Hence, Eg could be found at the first maximum on the lower energy side. It is observed that upon the heat treatment, the optical bandgap slightly decreases from 3.30 to 3.29 eV, probably due to the formation of new donor and/or acceptor levels within the ZnO energy gap, such as oxygen and zinc defects (similar value was also obtained by Tauc plot in Fig. S4) [23].

3.2. *Kinetic degradation of phenol, methylene blue (MB) and humic acid (HA)*

The photodegradation kinetics are intimately related to the type and intensity of irradiation sources, the bandgap energy of the photocatalyst, and the initial concentration of organic molecules, in addition to their molecular structures [16,38]. The latter could strongly affect the degradation rate due to the difference in the molecular geometry and bond energy of each component. Thus, the photocatalytic degradation was performed as a function of the type and the initial concentration of organic molecules under UVA irradiation of λ = 365 nm. The choice of a 365 nm irradiation wavelength is encouraged by the very low absorbance of organic molecules in the UVA range, limiting their degradation by photolysis.

3.2.1. *Effect of the initial concentrations*

Generally, the generation/migration of the photo-generated electron-hole pairs and subsequently their direct reaction (or that of the produced ROS) with the organic molecules occur successively [39]. In this respect, each of these steps may become rate-determining for the photocatalytic mechanisms. Hence, it was shown that at high initial concentrations (C_0 *in ppm*) of organic compounds ($K.C_0 \gg 1$, K refers to the adsorption equilibrium constant), the reaction rate is mainly governed by the generation and migration of e^--h^+ pairs, and thus it slowly increases with C_0 or remains constant (zero-order reaction) [40]. However, at relatively low initial concentrations ($1 \gg K.C_0$), the chemical reactions between the ROS and the molecules determine the reaction rate, which may be commonly noticed by a significant increase of the rate while increasing C_0 [40]. Thus, to predict the effect of the molecule structures on the degradation rate and oxidative mechanisms, a relatively low initial concentration range between 5 and 20 ppm was chosen. The photocatalytic degradations of phenol and humic acid (5, 10, and 20 ppm) were conducted at RT, under an irradiation source of 365

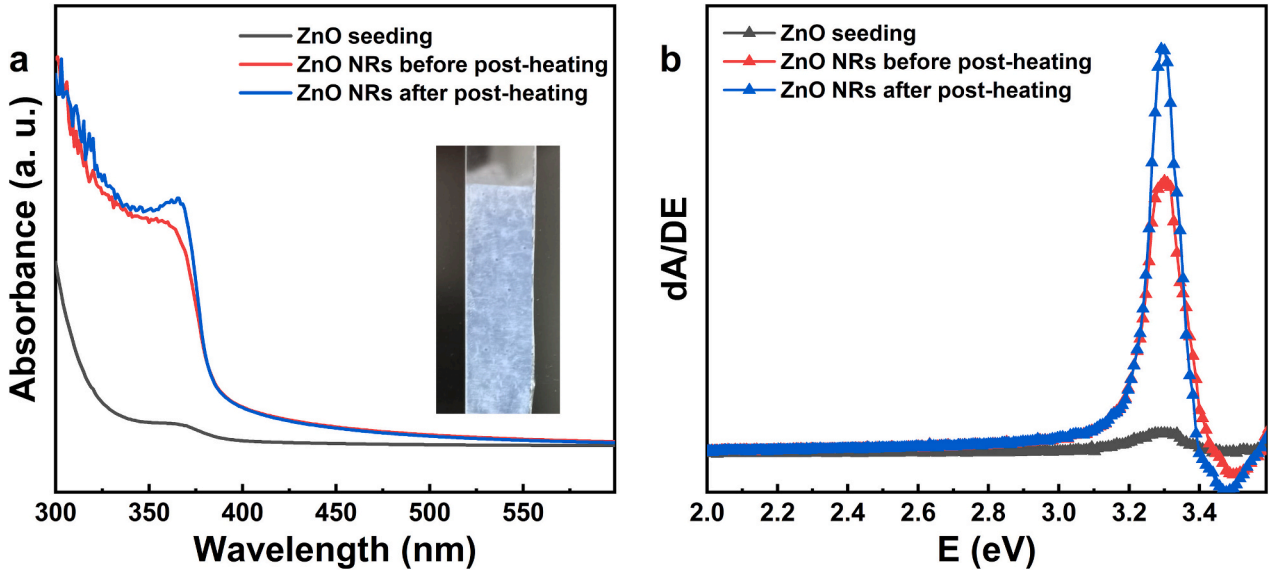

Fig. 4. **(a)** Room-temperature UV–vis absorbance spectrum of seeded ZnO, ZnO NRs after the hydrothermal growth, and ZnO NRs after the post-heat treatment in the air for 1 h. Inset: Digital photograph of the coated glass substrate with ZnO NRs after post-heat treatment, **(b)** Optical bandgap (Eg) obtained from the derivative of the absorbance spectrum of (c).

nm, and over an experimental time of 360 min, as shown in Figs. 5a & b.

The degradation kinetics were calculated from the Langmuir–Hinshelwood kinetic model (Eq.2) [41]:

$$r = -\frac{dC}{dt} = \frac{Kr.K.C}{1 + K.C} \tag{2}$$

where r, C, K, K_r, and t represent the reaction rate, molecule concentration at time t, adsorption equilibrium constant, limiting rate constant of reaction at maximum coverage, and contact time, respectively.

At small initial concentrations, ($K.C_0 \ll 1$), Eq. 2 may be simplified to the apparent rate order (Eq.3) [41]:

$$r = -\frac{dC}{dt} = K_{app}.C \tag{3}$$

where K_{app}, is the apparent degradation rate. Simple integration of this equation for $C = C_0$ at $t = 0$ gives Eq. 4:

$$ln\left(\frac{C_0}{C}\right) = K_{app}.t \tag{4}$$

Therefore, K_{app} may be obtained from the slope of the linear curve in the plot of $Ln\ (C_0/C)$ vs. t, where (C_0/C) is equal to (A_0/A) according to the Beer-Lambert law Eq.5.

$$A_0 = \varepsilon \times L \times C_0 \tag{5}$$

wherein A_0, A, C_0, C, ε & L refer respectively to the molecule light absorbance at t_0, molecule light absorbance at t, molecule concentration at t_0, molecule concentration at t, molar absorptivity, and length of the light path.

The photocatalytic degradation curves reveal that the kinetics of all the tested molecules obey the pseudo-first-order. In the absence of the

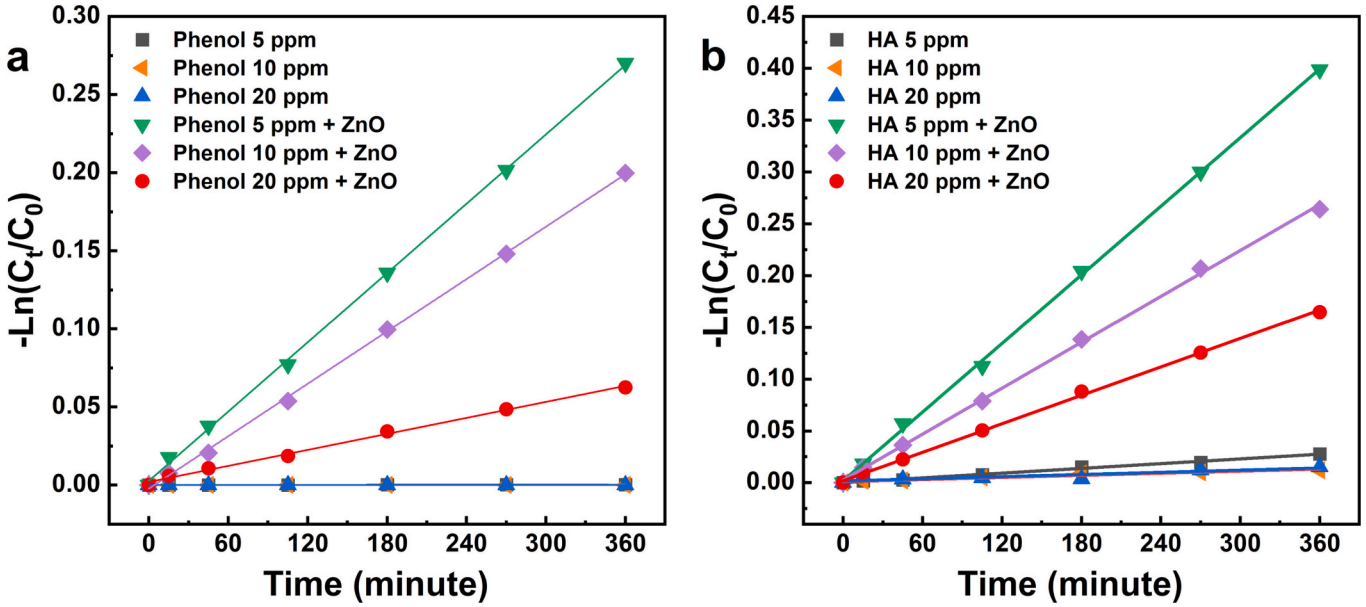

Fig. 5. Comparative photodegradation kinetics under UVA light of λ = 365 nm between C_0 = 5, 10, and 20 ppm of **(a)** Phenol and **(b)** Humic acid.

ZnO NRs, the blank solutions manifest insignificant K_{apps}. For instance, slightly detectable rates of ~6×10^{-7} min^{-1}, and 8×10^{-5} min^{-1}, are observed independently of the initial concentrations of phenol, and HA, respectively, indicating the negligible effect of photolysis (Fig. 5). However, this behavior is more pronounced in the case of MB where a K_{apps} of 1×10^{-4} min^{-1} is detected due to its higher absorbance in the UVA range (data not shown). After using the photocatalysts, the kinetic rates drastically increase, for different initial concentrations of the three pollutants. For example, the degradation rate of HA registers higher values of 0.0314 min^{-1} and 0.013 min^{-1} for 5 and 20 ppm, respectively, compared to the blank sample (8×10^{-5} min^{-1}). The decrease in the observed first-order rate constant at high concentration is certainly due to the occupation of all catalytic sites on the ZnO NRs surface. In addition, the non-polar characteristic of the majority of ZnO NRs surface, which exhibits low selectivity towards polar molecules [19] makes them a suitable material for this study.

3.2.2. *Influence of oxidative pathways on degradation rates*

The effect of the oxidative pathways on the degradation rate was investigated by choosing the lowest initial concentration of 5 ppm (shorter experimental time) for each of the organic molecules. The evolution of the UV–vis spectra of the MB, phenol, and HA is reported in Figs. 6a, b, and c for over 6 h of irradiation.

MB is generally characterized by 3 absorption bands (Fig. 6a). The first two are of high energy π – π* transition, corresponding to the B-Band and *E*-Band of the benzene ring, and located at λ ~ 247 and 293 nm, respectively [42]. The third peak, which is responsible for the blue color of the dissolved dye, corresponds to the low energy n – π* transition around 665 nm (where n is the free doublet on the nitrogen (N) and sulfur (S) atom of the chromophore groups, –C=N and –S=C, respectively) [43]. The observed shoulder at 605 nm refers to a vibronic transition 0–1 (level 0 of the ground state to level 1 of the excited state) [43]. To monitor the decomposition of the MB at the different molecular bonds, its photodegradation was tracked at the wavelengths 247, 293, and 665 nm. The same analytical method was applied to the phenol

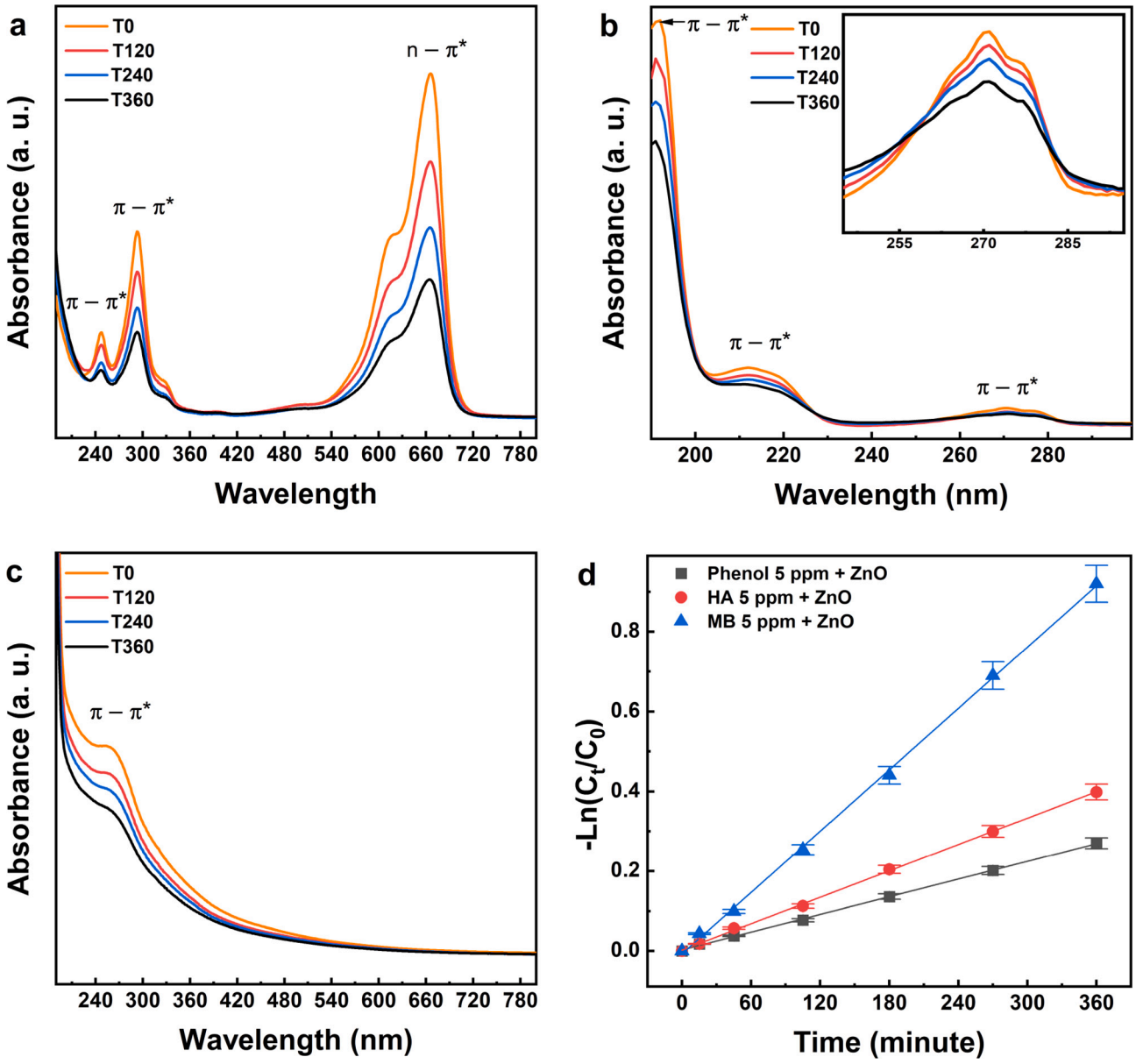

Fig. 6. UV–vis spectra of the UVA-photodegradation (λ = 365 nm), carried out over the as-prepared ZnO NRs film and plotted in function of experimental time for **(a)** 5 ppm MB **(b)** 5 ppm phenol, and **(c)** 5 ppm HA, **(d)** Comparative photodegradation kinetics of 5 ppm phenol (tracked at λ = 270 nm), 5 ppm HA (tracked at λ = 250 nm), and 5 ppm MB (tracked at λ = 665 nm).

molecule. Its photodegradation was then tracked at λ ~ 192, 212, and 270 nm, referring to the π – π* transitions of the E_1-Band, E_2-Band, and B-Band, respectively, as seen in Figure 6b[42]. The inset provides better visualization of the absorbance variation of the molecule at λ ~ 270 nm. As for the humic acid, the photodegradation of the molecule was studied at the single peak of λ ~ 250 nm. This peak corresponds to the π – π* electronic transitions of the polycyclic aromatic structure, including the phenolic group, aniline derivatives of benzoic acids, and polyenes (Fig. 6c) [44].

The photocatalytic degradation behavior, in Fig. 6d, reveals that the apparent degradation rates are the following: MB $K_{app_{min}}$ (0.0486 min^{-1}) > HA K_{app} (0.0314 min^{-1}) > Phenol K_{app} (0.0228 min^{-1}). $K_{app_{min}}$ of methylene blue represents the slowest measured rate at λ = 247 nm. These apparent rates constant are relatively higher than most of the reported kinetic data on various ZnO photocatalysts (Table S1). The apparent degradation rates for MB, HA, and phenol molecules that were recorded at the different absorbance peaks, are summarized in Table 2.

The degradation rates of HA, MB, and phenol are mainly governed by the amount of hydroxyl radicals and the chemical structures of the organic molecules [45–47]. The presence of these radicals was verified by measuring the photocatalytic efficiency of ZnO NRs before and after the addition of isopropanol (IPA) and potassium persulfate (KPS) quenching agents, in the case of MB (Fig. S3). Thus, adding the electron acceptor (KPS) slightly decreased the photocatalytic degradation of MB, whereas, using the OH radical scavenger is observed to significantly decrease the degradation kinetics of MB by 50%. Furthermore, as all the prepared ZnO NRs photocatalysts are highly homogeneous, the expected amount of hydroxyl radicals is similar for all experiments. Thus, the kinetic degradation rates are controlled by the complexity of pollutant structures. In this regard, the oxidative pathways of each molecule are estimated based on the obtained kinetic data from the UV–vis measurements. For instance, the changes in the UV–vis spectra of phenol show quite a similar degradation kinetic of ~0.0222 min^{-1} at the three absorbance peaks of 192, 212, and 270 nm (Table 2). This relatively low rate constant is due to the high dissociation molecular bond energy of ~97.12 kcal/mol[48]. As these peaks reflect the E_1-, E_2-, and B-band transitions, their reduction at the same rate indicates a complete transformation of the molecule. This is confirmed by the absence of any absorbance peaks that arise from the formation of intermediates (Fig. 6b). As reported elsewhere, the phenolic ring reacts with the $^{\bullet}OH$ to produce dihydroxy benzene, where its further oxidation either leads to a ring cleavage or the formation of quinone-like intermediates [49]. The faster degradation of the latter compared to phenol leads directly to its ring cleavage via a single oxidation step, giving oxalic and maleic acids [50]. Thus, the rupture of the phenolic ring is the rate-determining step [50]. The proposed mechanism of phenol degradation is illustrated in Fig. 7a.

On the other side, methylene blue demonstrates distinct rates of decline for its absorbance peaks at λ = 247, 293, and 665 nm, namely at ~0.0486, 0.06, and 0.0714 min^{-1}, respectively (Table 2). This implies that the decomposition of the conjugated system of phenothiazine chromophores (–C=N and –C=S) and the rest of the benzene structure follow different kinetics. When the MB molecules are attacked by the ROS, their degradation can undergo three different paths simultaneously. In consequence, the demethylation and *N*-demethylation of the MB were commonly observed at the beginning of the degradation due to the high vulnerability of the N–CH_3 bond that breaks down to form dimethylamino-intermediates [51]. Such molecules were frequently reported elsewhere, where intermediates such as formaldehyde (HCHO) or formic acid (HCOOH) were detected as soon as the degradation started [51,52]. In addition, the oxidation of the weak chromophore $C–S^+=C$ at very early stages of the degradation paves the way for the hemolytic cleavage of the thionine ring via a desulfurization pathway, resulting in various sulfoxide or sulphone intermediates [52]. Accordingly, Houas et al. (2001) reported the formation of sulfoxide intermediates and sulfate (SO_4^{2-}) ions during the beginning of MB photocatalytic degradation by titanium dioxide (TiO_2), confirming the opening of the thionine ring [53]. In addition to the desulphonation and demethylation reactions, the imino-group at the central heterocyclic rings is also prone to early oxidation, producing aniline and nitrate anions [51,52]. Moreover, the behavior of the MB in a highly rich medium with hydroxyl radicals was investigated by Huang et al. (2010) who also found that the molecule's degradation follows the same pathway [54]. Such an oxidation mechanism agrees with the bond dissociation energy (BDE) theory, wherein bonds of lower energy tend to decompose first: $CH_3–N(CH_3)C_6H_5$ (70.8 kcal/mol) < $C–S^+=C$ (76 kcal/mol) < C–N=C (87.4 kcal/mol) < $N(CH_3)_2–C_6H_5$ (93.2 kcal/mol) < $H_2N–C_6H_5$ (10.2.6 kcal/mol) [48,52,54,55].

Once the central ring is broken (Step 1, Fig. 7b), the resulting hydroxylated species, such as the relatively less stable hydroquinone or hydroquinone-like intermediates, are well known to undergo fast oxidation into acetic acids, maleic acids, oxalic acid, CO_2, and H_2O_2 (Step 2, Fig. 7b) [56]. Because these benzene rings are already hydroxylated with two or more –OH, their ring opening at this stage requires only one oxidation step, contrarily to phenol (which needs two or more oxidation steps). Consequently, due to this unique mechanism of MB degradation that bypasses the formation of highly stable species like phenol, methylene blue shows faster degradation kinetics. The proposed mechanism of MB degradation is visualized in Fig. 7b.

Similarly, the degradation of the macromolecular HA into smaller polyaromatic intermediates begins at its weakest bonds: C–N–C, and C–O–C[56]. Herein, the slower photodegradation rate of HA (0.0314 min^{-1}) compared to that of MB (0.0714 min^{-1}) indicates that the weakest molecular bond of MB (BDE of $C_6H_5–SC_6H_5 = 76 \pm 2$ kcal/mol) is oxidized faster than that of HA (BDE of $C_6H_5–O$ (C_6H_5) = 79.4 ± 2 kcal/mol) [56]. Hence, the HA molecule decomposes into various structures of polyaromatics, with absorption bands ranging between ~180 and 320 nm, corresponding to high-energy π – π* (K-, B-, and *E*-bands) transitions. Because the UV–vis spectrums of the HA and its intermediates are expected to overlap with each other, the real degradation kinetics may be hindered. For instance, the degradation of the HA byproducts was shown to proceed with ring cleavage steps to give new intermediates such as dibutyl phthalate, and glyoxylic acid [57]. Further oxidation of the latter can result in aliphatic species like octadecanoic or hexadecanoic acids [57]. Relatively small molecules i. e. the glyoxylic acid are also observed at advanced degradation time [57]. Although the photodegradation kinetics of humic acids appear to be slightly higher than those of phenol, the complete mineralization of the HA molecule and its byproducts generally follows a longer pathway. The formation of intermediates in the course of HA degradation is shown in Fig. 7c.

Table 2
Apparent degradation rates for MB, HA, and phenol molecules, recorded at the different absorbance peaks of each and normalized to the immersed specific area of ZnO NRs (~ 0.035 m^2).

λ (nm)	MB *Kapp* (min^{-1})	Phenol *Kapp* (min^{-1})	HA *Kapp* (min^{-1})	Transition Type
192	–	0.0228	–	π – π*
212	–	0.0222	–	π – π*
247	0.0486	–	–	π – π*
250	–	–	0.0314	π – π*
270	–	0.0228	–	π – π*
293	0.06	–	–	π – π*
665	0.0714	–	–	n – π*

4. Conclusion

In this study, we have demonstrated excellent photocatalytic degradation of methylene blue, humic acid, and phenol over ZnO nanorods synthesized by the hydrothermal growth method. Furthermore, a new approach to how the degradation rate of organic pollutants is correlated with their chemical structures and the bond dissociation

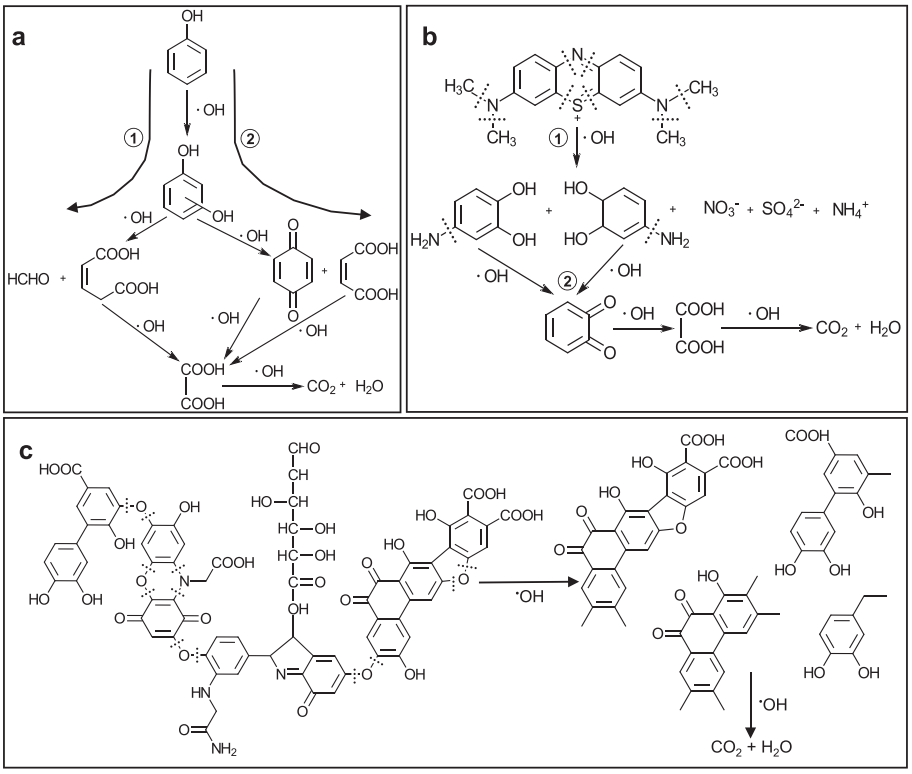

Fig. 7. Photocatalytic degradation pathway of dissolved **(a)** Phenol, **(b)** Methylene Blue, and **(c)** Humic acid. (For interpretation of the references to color in this figure legend, the reader is referred to the web version of this article.)

energies was investigated.

The lengths, and diameters of ZnO NRs were estimated by analyzing the SEM micrographs. An average diameter (w) of ~ 50 nm, a length (l) of ~ 1.55 μm, and a remarkably high ratio of l:w ~ 31 were registered. TEM analysis confirmed the uniform diameter of nanorods along its entire length, indicating their anisotropic growth along the ±c-axis direction. The EDS spectrum confirmed the presence of zinc (Zn), and oxygen (O) elements with an atomic ratio Zn:O of ~0.38:0.62 (± 0.017), deviating from the stoichiometric ratio of 1:1, and therefore indicating the potential presence of defects. The presence of these defects was also demonstrated by XPS with the presence of two peaks corresponding to the Zn $2p_{3/2}$ and Zn $2p_{1/2}$ correlated with the Zn—O bonding and 3 other peaks attributed to Zn—O bonding, O^{2-} ions in oxygen-deficient regions, and chemisorbed H_2O molecules respectively. These defects widely contribute to accelerating the photocatalytic degradation rate by increasing the number of trapped electrons/holes, and thus the formation of hydroxyl radical ($OH^{\bullet}$), superoxide radical ($O_2^{\bullet-}$), and other oxygenated radical species.

The photocatalytic degradation kinetics have been excessively studied by numerous works through several experimental parameters such as pH, molecules' initial concentrations, light source/intensity, and electron and hole scavengers. However, the impact of the chemical structure of organic pollutants on the degradation pathway mechanisms is timidly investigated. In this context, the influence of the oxidative pathway and the bond dissociation energies on the degradation rate was explored through three different chemical structures, including phenol, methylene blue, and humic acid. It was found that the photocatalytic efficiency is not necessarily related to the molecular sizes of organic pollutants. For instance, the molecular sizes of MB and HA are larger than those of phenol, however, they exhibit relatively higher degradation rates. More precisely, the removal of 90% of MB and HA is 3 and 1.4 times faster than the removal of phenol for the same initial concentration of 5 ppm. This behavior is explained by the difference in bond dissociation energies and structures between the concerned molecules. MB presents a relatively weak dissociation bond energy (~ 76 kcal/mol) at the thionine ring that tends to easily oxidize under the attack of ROS and dissociates into hydroxylated aromatics with more than two –OH groups. These highly hydroxylated intermediates require relatively less oxidation steps than phenol to achieve the ring cleavage, allowing therefore a faster removal process. In a similar way, the HA molecule possesses much weaker dissociation molecular bond energy (~ 79.4 kcal/mol), than phenol (minimum ~97.12 kcal/mol) and therefore shows more rapid degradation. Therefore, despite the complexity of the chemical structure of organic pollutant molecules, their degradation kinetics are mainly governed by the cleavage of the weakest molecular bonds and the number of oxidation steps. From this study, it was also concluded that ZnO nanorods photocatalysts have the potential to be used for the treatment of organic pollutants in water flow and the kinetic degradation rates can be predicted based on the chemical structure and the bond dissociation energies of molecules. In addition to the experimental data, theoretical models will be considered in the upcoming works to better investigate the degradation mechanism of oxide nanostructures and to optimize the degradation efficiency of the system.

CRediT authorship contribution statement

Elie A. Daher: Methodology, Investigation, Writing – original draft. **Cédric Boissière:** Methodology, Writing – review & editing. **Christel Laberty Robert:** Methodology, Writing – review & editing. **Wael Hamd:** Conceptualization, Methodology, Writing – review & editing, Supervision.

Declaration of Competing Interest

The authors declare that they have no known competing financial interests or personal relationships that could have appeared to influence the work reported in this paper.

Data availability

Data will be made available on request.

Acknowledgment

This work has been supported by CLAIM project: CLAIM, H2020-BG-2016–2017 [grant number 774586], “Cleaning Litter by Developing and Applying Innovative Methods in European Seas”. Mr. David Montero, Mr. Patrick Le Griel, and Mr. Mohamed Selmane are gratefully acknowledged for conducting SEM-FEG, TEM, and XRD measurements at Sorbonne University.

Appendix A. Supplementary data

Supplementary data to this article can be found online at https://doi.org/10.1016/j.catcom.2023.106807.

References

[1] T. Keijer, V. Bakker, J.C. Slootweg, Circular chemistry to enable a circular economy, Nat. Chem. 11 (3) (2019) 190–195, https://doi.org/10.1038/s41557-019-0226-9.
[2] A.M. El Hajj Chehade, E.A. Daher, J.C. Assaf, B. Riachi, W. Hamd, Simulation and optimization of hydrogen production by steam reforming of natural gas for refining and petrochemical demands in lebanon, Int. J. Hydrog. Energy 45 (58) (2020) 33235–33247, https://doi.org/10.1016/j.ijhydene.2020.09.077.
[3] S. Mohammadi, A. Kargari, H. Sanaeepur, K. Abbassian, A. Najafi, E. Mofarrah, Phenol removal from industrial wastewaters: a short review, Desalinat. Water Treat. 53 (8) (2015) 2215–2234, https://doi.org/10.1080/19443994.2014.883327.
[4] W.W. Anku, M.A. Mamo, P.P. Govender, Phenolic compounds in water: sources, reactivity, toxicity and treatment methods, in: M. Soto-Hernández, M. Palma-Tenango, M.R. del Garcia-Mateos (Eds.), Phenolic Compounds - Natural Sources, Importance and Applications, InTech, 2017, https://doi.org/10.5772/66927.
[5] Z. Wu, X. Zhang, J. Pang, X. Zhang, J. Li, J. Li, P. Zhang, Humic acid removal from water with PAC-Al $_{30}$: effect of calcium and kaolin and the action mechanisms, ACS Omega 5 (27) (2020) 16413–16420, https://doi.org/10.1021/acsomega.0c00532.
[6] E.M. Peña-Méndez, J. Havel, J. Patočka, Humic substances - compounds of still unknown structure: applications in agriculture, industry, environment, and biomedicine, J. Appl. Biomed. 3 (1) (2005) 13–24, https://doi.org/10.32725/jab.2005.002.
[7] A. Dobranskyte, R. Jugdaohsingh, C.R. McCrohan, E. Stuchlik, J.J. Powell, K. N. White, Effect of humic acid on water chemistry, bioavailability and toxicity of aluminium in the freshwater snail, lymnaea stagnalis, at neutral pH, Environ. Pollut. 140 (2) (2006) 340–347, https://doi.org/10.1016/j.envpol.2005.06.030.
[8] H. Zhang, M. Yang, Characterization of brominated disinfection byproducts formed during chloramination of fulvic acid in the presence of bromide, Sci. Total Environ. 627 (2018) 118–124, https://doi.org/10.1016/j.scitotenv.2018.01.215.
[9] M.-L. Cheng, H.-Y. Ho, Y.-W. Huang, F.-J. Lu, D.T.-Y. Chiu, Humic acid induces oxidative DNA damage, growth retardation, and apoptosis in human primary fibroblasts, Exp. Biol. Med. 228 (4) (2003) 413–423, https://doi.org/10.1177/153537020322800412.
[10] M. Hassanpour, H. Safardoust-Hojaghan, M. Salavati-Niasari, Degradation of methylene blue and rhodamine B as water pollutants via green synthesized Co_3O_4/ZnO nanocomposite, J. Mol. Liq. 229 (2017) 293–299, https://doi.org/10.1016/j.molliq.2016.12.090.
[11] I. Khan, K. Saeed, I. Zekker, B. Zhang, A.H. Hendi, A. Ahmad, S. Ahmad, N. Zada, H. Ahmad, L.A. Shah, T. Shah, I. Khan, Review on methylene blue: its properties, uses, toxicity and photodegradation, Water 14 (2) (2022) 242, https://doi.org/10.3390/w14020242.
[12] G. Crini, E. Lichtfouse, Advantages and disadvantages of techniques used for wastewater treatment, Environ. Chem. Lett. 17 (1) (2019) 145–155, https://doi.org/10.1007/s10311-018-0785-9.
[13] E.A. Daher, B. Riachi, J. Chamoun, C. Laberty-Robert, W. Hamd, New approach for designing wrinkled and porous ZnO thin films for photocatalytic applications, Colloids Surf. A Physicochem. Eng. Asp. 658 (2023), 130628, https://doi.org/10.1016/j.colsurfa.2022.130628.
[14] L. Xie, J.-G. Hao, H.-Q. Chen, Z.-X. Li, S.-Y. Ge, Y. Mi, K. Yang, K.-Q. Lu, Recent advances of nickel hydroxide-based cocatalysts in heterogeneous photocatalysis, Catal. Commun. 162 (2022), 106371, https://doi.org/10.1016/j.catcom.2021.106371.
[15] H.-Q. Chen, J.-G. Hao, Y. Wei, W.-Y. Huang, J.-L. Zhang, T. Deng, K. Yang, K.-Q. Lu, Recent developments and perspectives of cobalt sulfide-based composite materials in photocatalysis, Catalysts 13 (3) (2023) 544, https://doi.org/10.3390/catal13030544.
[16] K.M. Reza, A. Kurny, F. Gulshan, Parameters affecting the photocatalytic degradation of dyes using TiO_2: a review, Appl Water Sci 7 (4) (2017) 1569–1578, https://doi.org/10.1007/s13201-015-0367-y.
[17] H.A. Hamad, W.A. Sadik, M.M. Abd El-latif, A.B. Kashyout, M.Y. Feteha, Photocatalytic parameters and kinetic study for degradation of dichlorophenol-indophenol (DCPIP) dye using highly active mesoporous TiO_2 nanoparticles, J. Environ. Sci. 43 (2016) 26–39, https://doi.org/10.1016/j.jes.2015.05.033.
[18] R. Yanagi, T. Zhao, D. Solanki, Z. Pan, S. Hu, Charge separation in photocatalysts: mechanisms, physical parameters, and design principles, ACS Energy Lett. 7 (1) (2022) 432–452, https://doi.org/10.1021/acsenergylett.1c02516.
[19] V. Rogé, C. Guignard, G. Lamblin, F. Laporte, I. Fechete, F. Garin, A. Dinia, D. Lenoble, Photocatalytic degradation behavior of multiple xenobiotics using MOCVD synthesized ZnO nanowires, Catal. Today 306 (2018) 215–222, https://doi.org/10.1016/j.cattod.2017.05.088.
[20] M.A. Mahmood, S. Jan, I.A. Shah, I. Khan, Growth parameters for films of hydrothermally synthesized one-dimensional nanocrystals of zinc oxide, Int. J. Photoenergy 2016 (2016) 1–12, https://doi.org/10.1155/2016/3153170.
[21] A. Renaud, L. Cario, X. Rocquefelte, P. Deniard, E. Gautron, E. Faulques, T. Das, F. Cheviré, F. Tessier, S. Jobic, Unravelling the origin of the giant Zn deficiency in wurtzite type ZnO nanoparticles, Sci. Rep. 5 (1) (2015) 12914, https://doi.org/10.1038/srep12914.
[22] K.M. Wong, Y. Fang, A. Devaux, L. Wen, J. Huang, L. De Cola, Y. Lei, Assorted analytical and spectroscopic techniques for the optimization of the defect-related properties in size-controlled ZnO nanowires, Nanoscale 3 (11) (2011) 4830, https://doi.org/10.1039/c1nr10806a.
[23] T. Bora, P. Sathe, K. Laxman, S. Dobretsov, J. Dutta, Defect engineered visible light active ZnO nanorods for photocatalytic treatment of water, Catal. Today 284 (2017) 11–18, https://doi.org/10.1016/j.cattod.2016.09.014.
[24] S. Baruah, M.A. Mahmood, M.T.Z. Myint, T. Bora, J. Dutta, Enhanced visible light photocatalysis through fast crystallization of zinc oxide nanorods, Beilstein J. Nanotechnol. 1 (2010) 14–20, https://doi.org/10.3762/bjnano.1.3.
[25] A. Sulciute, K. Nishimura, E. Gilshtein, F. Cesano, G. Viscardi, A.G. Nasibulin, Y. Ohno, S. Rackauskas, ZnO nanostructures application in electrochemistry: influence of morphology, J. Phys. Chem. C 125 (2) (2021) 1472–1482, https://doi.org/10.1021/acs.jpcc.0c08459.
[26] D. Pugliese, F. Bella, V. Cauda, A. Lamberti, A. Sacco, E. Tresso, S. Bianco, A chemometric approach for the sensitization procedure of ZnO flowerlike microstructures for dye-sensitized solar cells, ACS Appl. Mater. Interfaces 5 (21) (2013) 11288–11295, https://doi.org/10.1021/am403527m.
[27] C. Gu, L. Shanshan, J. Huang, C. Shi, J. Liu, Preferential growth of long ZnO nanowires and its application in gas sensor, Sensors Actuators B Chem. 177 (2013) 453–459, https://doi.org/10.1016/j.snb.2012.11.044.
[28] S. Kovačič, A. Anžlovar, B. Erjavec, G. Kapun, N.B. Matsko, M. Žigon, E. Žagar, A. Pintar, C. Slugovc, Macroporous ZnO foams by high internal phase emulsion technique: synthesis and catalytic activity, ACS Appl. Mater. Interfaces 6 (21) (2014) 19075–19081, https://doi.org/10.1021/am5050482.
[29] M.F. Smith, S. Limwichean, M. Horprathum, J. Chaiprapa, W.W. Aye, C. Chananonnawathorn, V. Patthanasettakul, P. Eiamchai, N. Nuntawong, A. Klamchuen, P. Songsiriritthigul, Determination of density and specific surface area of nanostructured zinc oxide films by X-ray fluorescence and scanning electron microscopy, Thin Solid Films 751 (2022), 139207, https://doi.org/10.1016/j.tsf.2022.139207.
[30] J. Zhang, S. Wang, Y. Wang, M. Xu, H. Xia, S. Zhang, W. Huang, X. Guo, S. Wu, ZnO hollow spheres: preparation, characterization, and gas sensing properties, Sensors Actuators B Chem. 139 (2) (2009) 411–417, https://doi.org/10.1016/j.snb.2009.03.014.
[31] A. Sugunan, H.C. Warad, M. Boman, J. Dutta, Zinc oxide nanowires in chemical bath on seeded substrates: role of hexamine, J. Sol-Gel Sci. Technol. 39 (1) (2006) 49–56, https://doi.org/10.1007/s10971-006-6969-y.
[32] J. Singh, S. Kaur, G. Kaur, S. Basu, M. Rawat, Biogenic ZnO nanoparticles: a study of blueshift of optical band gap and photocatalytic degradation of reactive yellow 186 dye under direct sunlight, Green Proc. Synth. 8 (1) (2019) 272–280, https://doi.org/10.1515/gps-2018-0084.
[33] M.L. da Silva-Neto, M.C.A. de Oliveira, C.T. Dominguez, R.E.M. Lins, N. Rakov, C. B. de Araújo, L.S. de Menezes, H.P. de Oliveira, A.S.L. Gomes, UV random laser emission from flexible ZnO-Ag-enriched electrospun cellulose acetate fiber matrix, Sci. Rep. 9 (1) (2019) 11765, https://doi.org/10.1038/s41598-019-48056-w.
[34] S, M.; N, H.; P.P, V, In vitro biocompatibility and antimicrobial activities of zinc oxide nanoparticles (ZnO NPs) prepared by chemical and green synthetic route— A comparative study, BioNanoScience 10 (1) (2020) 112–121, https://doi.org/10.1007/s12668-019-00698-w.
[35] M.F. Malek, M.H. Mamat, Z. Khusaimi, M.Z. Sahdan, M.Z. Musa, A.R. Zainun, A. B. Suriani, N.D. Md Sin, S.B. Abd Hamid, M. Rusop, Sonicated sol–gel preparation of nanoparticulate ZnO thin films with various deposition speeds: the highly preferred c-Axis (002) orientation enhances the final properties, J. Alloys Compd. 582 (2014) 12–21, https://doi.org/10.1016/j.jallcom.2013.07.202.
[36] N. Hidayat, Sunaryono, A. Taufiq, R.E. Saputro, Kusnunnahari, L. Chuenchom, Temperature Effect on Crystal Structures, Morphological Shapes, and Functional Groups of Zinc Oxide; Tangerang Selatan, Indonesia, 2020, p. 030017, https://doi.org/10.1063/5.0000910.
[37] P. Poulopoulos, S. Baskoutas, S.D. Pappas, C.S. Garoufalis, S.A. Droulias, A. Zamani, V. Kapaklis, Intense quantum confinement effects in Cu_2O thin films, J. Phys. Chem. C 115 (30) (2011) 14839–14843, https://doi.org/10.1021/jp203145n.
[38] S. Wang, F. Teng, Y. Zhao, Effect of the molecular structure and surface charge of a bismuth catalyst on the adsorption and photocatalytic degradation of dye mixtures, RSC Adv. 5 (93) (2015) 76588–76598, https://doi.org/10.1039/C5RA14931B.

[39] W. Hamd, E.A. Daher, T.S. Tofa, J. Dutta, Recent advances in photocatalytic removal of microplastics: mechanisms, kinetic degradation, and reactor design, Front. Mar. Sci. 9 (2022), 885614, https://doi.org/10.3389/fmars.2022.885614.
[40] D. Chen, Photocatalytic kinetics of phenol and its derivatives over UV irradiated TiO_2, Appl. Catal. B Environ. 23 (2–3) (1999) 143–157, https://doi.org/10.1016/S0926-3373(99)00068-5.
[41] K.V. Kumar, K. Porkodi, F. Rocha, Langmuir–hinshelwood kinetics – A theoretical study, Catal. Commun. 9 (1) (2008) 82–84, https://doi.org/10.1016/j.catcom.2007.05.019.
[42] L.D.S. Yadav, Organic Spectroscopy, Springer Netherlands, Dordrecht, 2005, https://doi.org/10.1007/978-1-4020-2575-4.
[43] D. Heger, J. Jirkovský, P. Klán, Aggregation of methylene blue in frozen aqueous solutions studied by absorption spectroscopy, J. Phys. Chem. A 109 (30) (2005) 6702–6709, https://doi.org/10.1021/jp050439j.
[44] F.J. Rodríguez, P. Schlenger, M. García-Valverde, Monitoring changes in the structure and properties of humic substances following ozonation using UV–Vis, FTIR and 1 H NMR techniques, Sci. Total Environ. 541 (2016) 623–637, https://doi.org/10.1016/j.scitotenv.2015.09.127.
[45] J. Singh, S. Juneja, S. Palsaniya, Ashis K. Manna, R.K. Soni, J. Bhattacharya, Evidence of oxygen defects mediated enhanced photocatalytic and antibacterial performance of ZnO nanorods, Colloids Surf. B: Biointerfaces 184 (2019), 110541, https://doi.org/10.1016/j.colsurfb.2019.110541.
[46] J. Al-Sabahi, T. Bora, M. Al-Abri, J. Dutta, Efficient visible light photocatalysis of benzene, toluene, ethylbenzene and xylene (BTEX) in aqueous solutions using supported zinc oxide nanorods, PLoS One 12 (12) (2017), e0189276, https://doi.org/10.1371/journal.pone.0189276.
[47] Y. Wang, P.-H. Yuan, C.-M. Fan, Y. Wang, G.-Y. Ding, Y.-F. Wang, Preparation of zinc titanate nanoparticles and their photocatalytic behaviors in the photodegradation of humic acid in water, Ceram. Int. 38 (5) (2012) 4173–4180, https://doi.org/10.1016/j.ceramint.2012.01.078.
[48] M. Leopoldini, T. Marino, N. Russo, M. Toscano, Antioxidant properties of phenolic compounds: H-atom versus electron transfer mechanism, J. Phys. Chem. A 108 (22) (2004) 4916–4922, https://doi.org/10.1021/jp037247d.
[49] L.G. Devi, K.E. Rajashekhar, A kinetic model based on non-linear regression analysis is proposed for the degradation of phenol under UV/solar light using nitrogen doped TiO_2, J. Mol. Catal. A Chem. 334 (1–2) (2011) 65–76, https://doi.org/10.1016/j.molcata.2010.10.025.
[50] N. Wang, L. Zhu, Y. Huang, Y. She, Y. Yu, H. Tang, Drastically enhanced visible-light photocatalytic degradation of colorless aromatic pollutants over TiO_2 via a charge-transfer-complex path: a correlation between chemical structure and degradation rate of the pollutants, J. Catal. 266 (2) (2009) 199–206, https://doi.org/10.1016/j.jcat.2009.06.006.
[51] Q. Wang, S. Tian, P. Ning, Degradation mechanism of methylene blue in a heterogeneous fenton-like reaction catalyzed by ferrocene, Ind. Eng. Chem. Res. 53 (2) (2014) 643–649, https://doi.org/10.1021/ie403402q.
[52] S. Su, Y. Liu, X. Liu, W. Jin, Y. Zhao, Transformation pathway and degradation mechanism of methylene blue through β-FeOOH@GO catalyzed photo-fenton-like system, Chemosphere 218 (2019) 83–92, https://doi.org/10.1016/j.chemosphere.2018.11.098.
[53] A. Houas, Photocatalytic degradation pathway of methylene blue in water, Appl. Catal. B Environ. 31 (2) (2001) 145–157, https://doi.org/10.1016/S0926-3373(00)00276-9.
[54] F. Huang, L. Chen, H. Wang, Z. Yan, Analysis of the degradation mechanism of methylene blue by atmospheric pressure dielectric barrier discharge plasma, Chem. Eng. J. 162 (1) (2010) 250–256, https://doi.org/10.1016/j.cej.2010.05.041.
[55] Y.-R. Luo, Handbook of Bond Dissociation Energies in Organic Compounds, 0 ed, CRC Press, 2002, https://doi.org/10.1201/9781420039863.
[56] S.C. Moldoveanu, General information about pyrolysis, in: Pyrolysis of Organic Molecules, Elsevier, 2019, pp. 1–33, https://doi.org/10.1016/B978-0-444-64000-0.00001-9.
[57] A. Li, X. Zhao, H. Liu, J. Qu, Characteristic transformation of humic acid during photoelectrocatalysis process and its subsequent disinfection byproduct formation potential, Water Res. 45 (18) (2011) 6131–6140, https://doi.org/10.1016/j.watres.2011.09.012.